ADVANCED MATERIALS
www.advmat.de

Matrix Viscoelasticity Controls Differentiation of Human Blood Vessel Organoids into Arterioles and Promotes Neovascularization in Myocardial Infarction

Dayu Sun, Kunyu Zhang, Feiyang Zheng, Guanyuan Yang, Mingcan Yang, Youqian Xu, Yinhua Qin, Mingxin Lin, Yanzhao Li, Ju Tan, Qiyu Li, Xiaohang Qu, Gang Li, Liming Bian, and Chuhong Zhu**

Stem cell-derived blood vessel organoids are embedded in extracellular matrices to stimulate vessel sprouting. Although vascular organoids in 3D collagen I-Matrigel gels are currently available, they are primarily capillaries composed of endothelial cells (ECs), pericytes, and mesenchymal stem-like cells, which necessitate mature arteriole differentiation for neovascularization. In this context, the hypothesis that matrix viscoelasticity regulates vascular development is investigated in 3D cultures by encapsulating blood vessel organoids within viscoelastic gelatin/β-CD assembly dynamic hydrogels or methacryloyl gelatin non-dynamic hydrogels. The vascular organoids within the dynamic hydrogel demonstrate enhanced angiogenesis and differentiation into arterioles containing smooth muscle cells. The dynamic hydrogel mechanical microenvironment promotes vascular patterning and arteriolar differentiation by elevating notch receptor 3 signaling in mesenchymal stem cells and downregulating platelet-derived growth factor B expression in ECs. Transplantation of vascular organoids in vivo, along with the dynamic hydrogel, leads to the reassembly of arterioles and restoration of cardiac function in infarcted hearts. These findings indicate that the viscoelastic properties of the matrix play a crucial role in controlling the vascular organization and differentiation processes, suggesting an exciting potential for its application in regenerative medicine.

1. Introduction

Among noncommunicable diseases, cardiovascular disease (CVD) is the leading cause of morbidity and mortality worldwide.[1] Myocardial infarction (MI), defined pathologically as myocardial cell death due to prolonged ischemia, is one form of CVD.[2] While reperfusion therapy can adequately restore major epicardial vessel patency, ischemic endothelial damage and dislodging of thrombotic debris from the primary lesion frequently lead to microvascular obstruction. This-"no-reflow" phenomenon is associated with poor MI healing.[3] Without a necessary nutritional supply, cardiomyocytes are unlikely to survive or function well during injury.[4]

Despite the efforts of the heart to self-repair through an intrinsic neovascularization response after ischemic injury, the speed and extent of this response are insufficient to prevent extensive damage to the myocardium. The human heart has high metabolic needs and is supplied with

D. Sun, F. Zheng, G. Yang, M. Yang, Y. Xu, Y. Qin, Y. Li, J. Tan, Q. Li, X. Qu, G. Li, C. Zhu
Department of Anatomy
Engineering Research Center of the Ministry of Education for Tissue and Organ Regeneration and Manufacturing
Engineering Research Center for Organ Intelligent Biological Manufacturing of Chongqing
Third Military Medical University
Chongqing 400038, P. R. China
E-mail: zhuch99@tmmu.edu.cn

D. Sun, F. Zheng, G. Yang, M. Yang, Y. Xu, Y. Qin, Y. Li, J. Tan, Q. Li, X. Qu, G. Li, C. Zhu
State Key Laboratory of Trauma and Chemical Poisoning
Chongqing 400038, P. R. China

K. Zhang, M. Lin, L. Bian
School of Biomedical Sciences and Engineering
Guangzhou International Campus
South China University of Technology
Guangzhou 511442, P. R. China
E-mail: bianlm@scut.edu.cn

K. Zhang, M. Lin, L. Bian
National Engineering Research Center for Tissue Restoration and Reconstruction
Guangdong Provincial Key Laboratory of Biomedical Engineering
South China University of Technology
Guangzhou 510006, P. R. China

The ORCID identification number(s) for the author(s) of this article can be found under https://doi.org/10.1002/adma.202410802

DOI: 10.1002/adma.202410802

a dense network of 2000–3000 capillaries mm^{-2}.[5] Endogenous collateral arteries develop as an adaptive response to provide functional bypasses that bridge pre-existing arteries.[6] In mammals, endothelial cells (ECs) can migrate and reassemble into collateral arteries in neonatal mouse hearts after MI; however, this process is nearly absent in adults. The transplantation of endothelial progenitor cells (EPCs) into the ischemic myocardium results in increased capillary density.[7] Injection of EPCs into infarcted hearts restores cardiac function and increases the density of CD31+ vessel structures.[8] However, EPCs alone are insufficient to provide the complex cellular composition required for artery formation, owing to the lack of mural cells (MCs). Therefore, a strategy to promote arterial reassembly in adults by transplanting both EPCs and MCs would offer a new opportunity to promote cardiac neovascularization in adult individuals with CVD.

Organoids undergo self-organization through spatially restricted lineage commitment, resembling in vivo processes.[9] They originate from stem cells that replicate human development[10] in contrast to traditional strategies that combine various terminally differentiated cell types. Wimmer et al. generated the first 3D human blood vessel organoids (hBVOs) containing both ECs and pericytes by inducing mesodermal and vascular differentiation.[11,12] Following embedding in the collagen I-Matrigel matrix, the organoids self-organize to form vascular sprouting and capillary networks. hESC-derived hBVOs injected into the ischemic region of MI mouse models show higher therapeutic potential than single early vascular cells.[13] The main challenges in the field of blood vessel organoids include the absence of vascular smooth muscle cells (SMCs)[14] and the inability to generate larger vessels in vitro, especially arterioles and arteries.

Matrigel is commonly utilized in the induction of various organoids, such as cerebral,[15,16] intestinal,[17] and bone marrow organoids.[18] It is also used as an extracellular matrix (ECM) to induce the vessel sprouting of hBVOs. Matrigel is derived from the secretions of Engelbreth–Holm–Swarm mouse sarcoma cells, posing risks of potential immunogen and pathogen transfer.[19] Synthetic ECM analogs offer a promising alternative to native matrices, as they allow control over the mechanical properties, functionality, and degradation rate. Dynamic hydrogels with tunable stress relaxation have been designed to emulate the natural ECM properties and explore their biological effects.[20] In our previous studies, we discovered that dynamically crosslinked hydrogels with high dissociation rate constants enhance the spreading, assembly, and differentiation of encapsulated human mesenchymal stem cells (MSCs).[21] Compared with covalently crosslinked hydrogels, dynamic hydrogels can boost the proliferation and self-renewal of mouse ESCs in 3D culture.[22] Nevertheless, there is limited knowledge regarding the regulation of blood vessel development or differentiation by viscoelastic hydrogels.

In this study, we utilized a gelatin-based structurally dynamic hydrogel to investigate the effect of matrix viscoelasticity on vascular sprouting and maturation of vascular structures (**Scheme 1**). The results revealed that the dynamic hydrogel (D-hydrogel) outperformed the nondynamic hydrogel (ND-hydrogel) in promoting hBVO angiogenesis. Additionally, the hBVOs differentiated into arterioles in the D-hydrogel and capillaries in the ND-hydrogel. Co-injection of hBVOs with the D-hydrogel could restore cardiac function in infarcted hearts and facilitate arteriole reassembly in vivo. The methodology presented here can facilitate the maturation of blood vessels into arterioles, offering the potential to enhance neovascularization and contribute to ischemic repair during clinical translation.

2. Results

2.1. The Supramolecular GelCD D-Hydrogel Exhibits Promising Dynamic Properties

The synthesized photocrosslinkable acryloyl β-cyclodextrin (Ac-β-CD) with an average degree of acryloyl substitution of 1.2 (Figure S1, Supporting Information) was first allowed to assemble with the aromatic residues of gelatin (e.g., phenylalanine, tyrosine, and tryptophan) via host–guest interactions. The formation of supramolecular gelatin/β-CD assembly (GelCD) D-hydrogels was then initiated by the polymerization of the Ac-β-CDs. At the molecular level, this host–guest interaction is characterized by a higher dissociation rate, which supports more frequent network remodeling, thereby enhancing the viscoelasticity of the D-hydrogel. Different concentration combinations of Ac-β-CD and gelatin were tested, and 8% gelation with 10% Ac-β-CD showed reasonable mechanical properties and stability and thus was used in the following study (Figure S2, Supporting Information). The rheological properties of the two hydrogel groups were evaluated using a hybrid rheometer. In the strain-time scan sweep (**Figure 1a**), while the GelCD D-hydrogel and the methacryloyl gelatin (GelMA) ND-hydrogel exhibited similar energy storage moduli over 180 s, the loss modulus of the D-hydrogel group was consistently higher than that of the ND-hydrogel group. This trend is further supported by scans of the linear viscoelastic region (Figure S3, Supporting Information). This indicated that the D-hydrogel had a more dynamic network and exhibited better fluidic properties. Frequency scanning experiments further demonstrated the frequency-dependent viscoelastic properties unique to D-hydrogels (Figure 1b). This may be due to the formation of a host–guest interaction between the structural residues of the benzene ring carried on the side chain of gelatin and β-cyclodextrin (β-CD). We further investigated the dynamic properties of the hydrogels through stress-relaxation experiments (Figure 1c). The half-stress relaxation time is defined as the time required for the stress to decrease to 50% of its initial value under a constant compressive strain. The D-hydrogel had a very fast stress relaxation rate, with a half-stress relaxation time of ≈11 s (Figure 1d), whereas the D-hydrogel exhibited similar Young's modulus to that of the ND-hydrogel (Figure 1e). These effects may be because the highly dynamic network structure of D-hydrogel can dissipate the external energy much faster than that of ND-hydrogel. To demonstrate the injectability of the D-hydrogels, alternate-step strain-amplitude sweep experiments were performed (Figure 1f). The results showed that D-hydrogel possessed shear-thinning and self-healing properties. Based on these results, we began injectability experiments, as shown in Figure 1g. A dye was used to color the hydrogel red, loaded into a syringe, and then injected into different molds via a 27G needle. The extruded hydrogels quickly formed the corresponding shapes and were successfully demolded. These observations

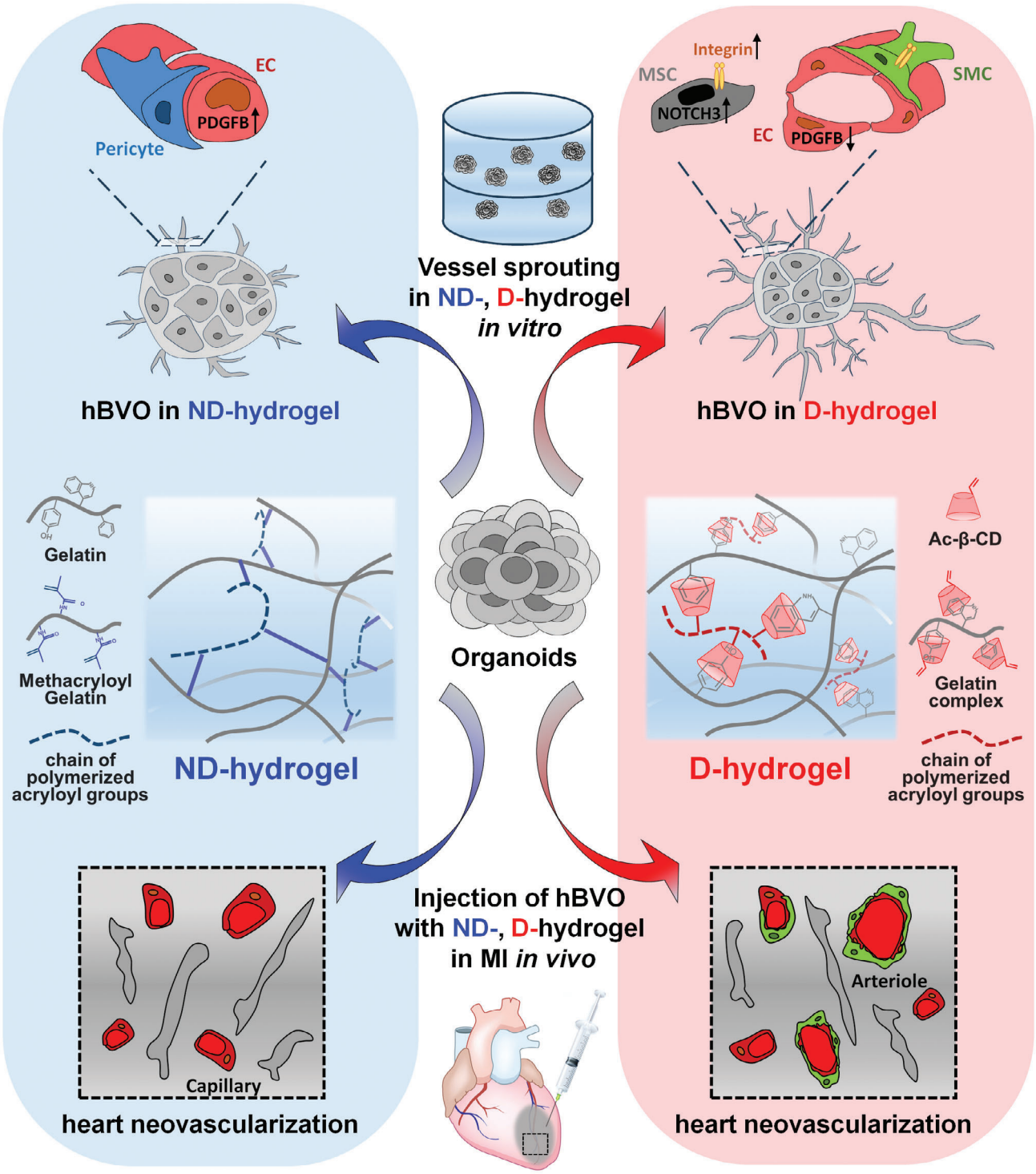

Scheme 1. The regulation of hBVO differentiation by manipulating the matrix viscoelasticity of the embedding hydrogels and its application in post-myocardial infarction treatment.

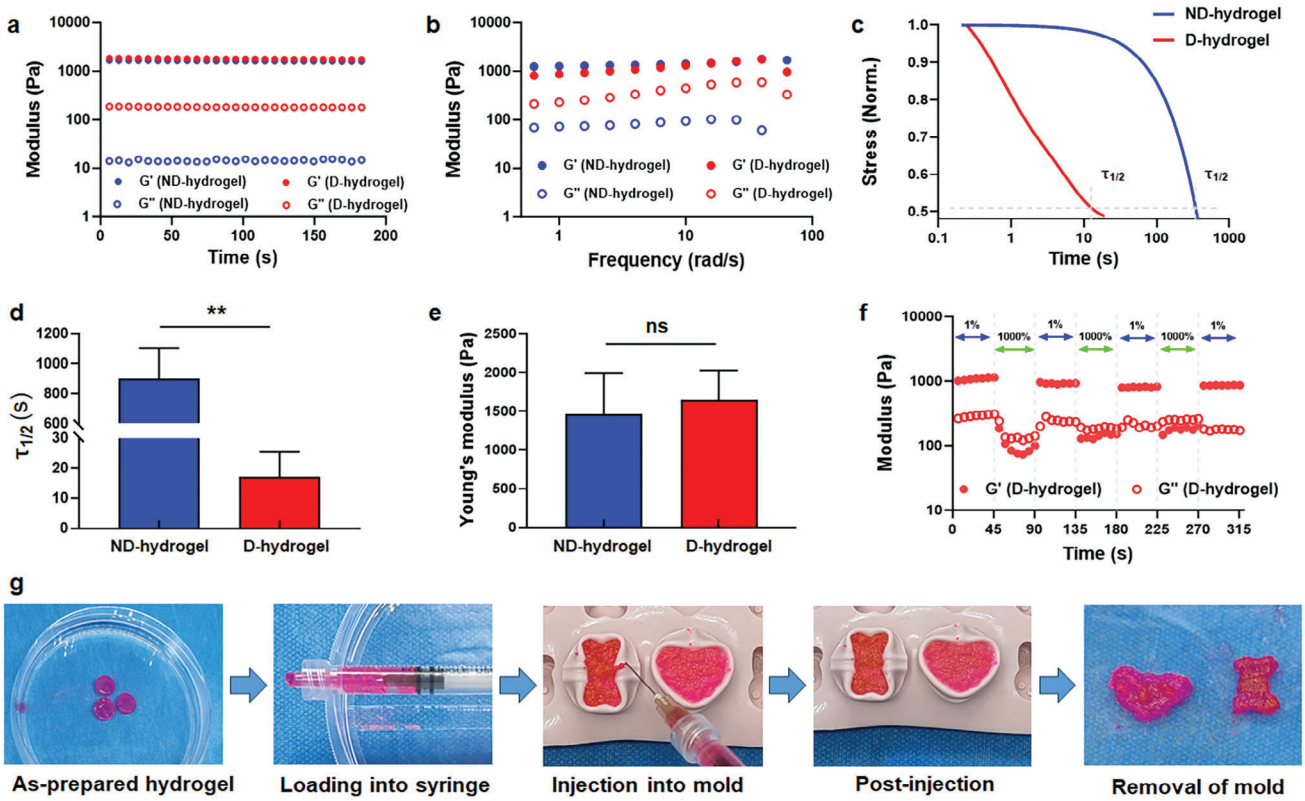

Figure 1. Characterization of dynamic network hydrogels and non-dynamic network hydrogels. a–e) The mechanical properties comparison between the non-dynamic (ND)-hydrogel and dynamic (D)-hydrogel. a) The storage (G′) and loss (G″) moduli of ND-hydrogel and D-hydrogel collected from the time sweep of dynamic rheology study. b) The G′ and G″ of the ND- and D-hydrogels from frequency sweep tests recorded at a constant strain of 0.1% and with some different frequencies. c) Stress relaxation test for ND-hydrogel and D-hydrogel under 15% peak compressive strain. d) $\tau_{1/2}$ (the time taken to relax half of the maximum stress) of ND- and D-hydrogels ($n = 3$). e) Average Young's modulus of ND- and D-hydrogels ($n = 3$). f) The rapid "sol–gel" transition property of D-hydrogel under alternating high (1000%) and low (1%) shear strains at 37 °C. g) Demonstration of the injectability and moldability of the D-hydrogel. ** $p < 0.01$; *** $p < 0.001$; ns, not significant.

collectively demonstrate the excellent dynamic characteristics and injectability of the D-hydrogel.

2.2. Human Blood Vessel Organoid Self-Organization and Sprouting Depend on Matrix Viscoelasticity

A multistep protocol was utilized to generate vascular organoids from human pluripotent stem cells (hPSCs).[11] hPSCs were first aggregated in anti-adhesion-treated AggreWells for 1 d to form embryonic bodies (EBs). EBs were then induced to form the mesoderm via BMP-4 stimulation and Wnt activation using CHIR99021. Subsequently, vascular differentiation was induced using a combination of VEGF-A and forskolin. Subsequently, the organoids were encapsulated in a hydrogel to facilitate vascular sprouting driven by VEGF-A and FGF-2 stimulation in the presence of serum. To explore the impact of viscoelasticity on vessel development and maturation, organoids were embedded in the ND- or D-hydrogels on day 6 of the vessel sprouting protocol (**Figure 2a**). Calcein-AM/PI staining was performed to test the viability of hBVOs post blue light exposure, with no significant damage observed (Figure S4, Supporting Information). During the vascular sprouting period, the morphology of the organoids in the hydrogels was monitored on days 7, 9, and 11. Some sporadic sprouts were observed on day nine in both groups, whereas a larger number of vascular sprouts were observed in the D-hydrogel group on day 11 (Figure 2b). The area of hBVO in the D-hydrogel group gradually increased from days 7 to 11, while no significant difference was found in the ND-hydrogel group. The maximum length of hBVO followed a similar trend, except that the maximum length increased in the ND-hydrogel group between days 7 and 9. Compared with the ND-hydrogel group, the D-hydrogel group exhibited significant increases in both the area and maximum length of the overall hBVOs on days 9 and 11 (Figure 2c). The ECs of the hBVOs in the ND-hydrogel group were densely located around the spherical surface of the organoids, whereas the ECs in the D-hydrogel extended into the dynamic 3D matrix. Ultrastructurally, the lumen structure and typical tight junctions formed between the ECs were observed within the vascular organoids (Figure 2d). The intracellular lumen that formed inside a single EC in the ND-hydrogel resembled a capillary, whereas the larger lumen surrounded by multiple ECs in the D-hydrogel corresponded to larger vessels. This suggests that the viscoelasticity of the hydrogel plays a crucial role in regulating the size and organization of the vascular structures in hBVOs. In addition, typical EC structures,

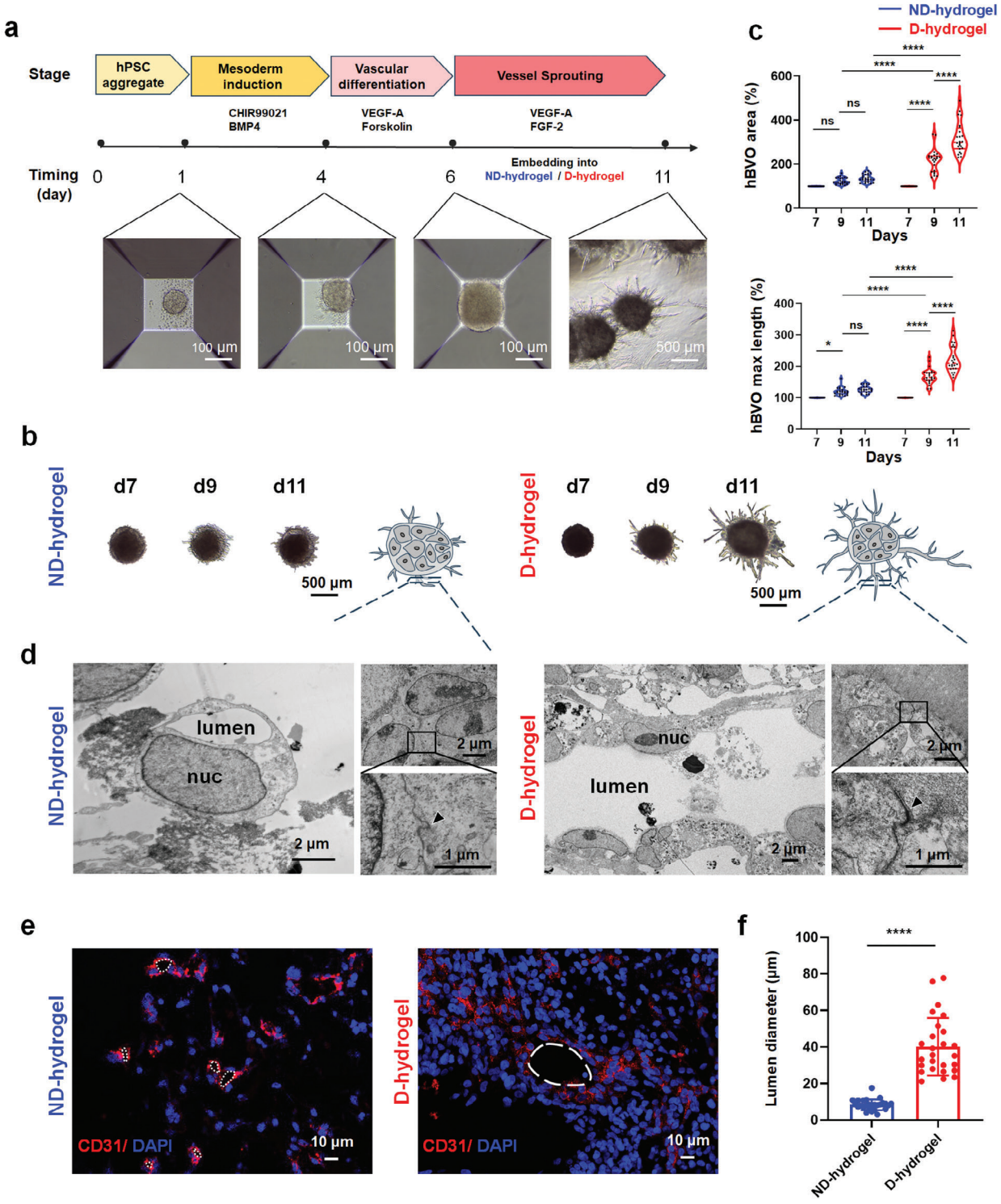

Figure 2. General features of hBVO in ND- and D-hydrogels. a) Schematic depicting the protocols used for the differentiation of human pluripotent stem cells into blood vessel organoids. b) Representative light micrographic images of hBVO encapsulated in ND-hydrogel and D-hydrogel on days 7, 9, and 11. Scale bars, 500 μm. c) Quantitative analysis of the area and max length of human blood vessel organoids (hBVOs) embedded in ND- and D-hydrogels at days 7, 9, and 11 ($n = 24$, from three different batches). d) Transmission electron microscopy of the lumen structure (left panel) and tight junctions (right panel, black arrowheads) in vascular organoids. Scale bar, 2 μm (left and top right), 1 μm (bottom). e) Representative immunofluorescence staining with CD31 to show the hBVO vascular lumens in ND-hydrogel (white dots) and D-hydrogel (white dashed lines). Scale bars, 10 μm. f) Quantitative analysis of the lumen diameter of hBVOs from the ND- and D-hydrogel groups. ($n = 26$, from three different batches). * $p < 0.05$; **** $p < 0.0001$; ns, not significant.

including microvilli and Weibel–Palade bodies, were observed (Figure S5, Supporting Information). Hematoxylin-eosin (HE) staining of hBVO sprouting revealed the cross-sectional and longitudinal structures of the vascular lumens (Figure S6, Supporting Information). Immunostaining with CD31 was performed to show the ECs lining the lumens (Figure 2e), and the hBVO lumen diameters were measured. It was observed that the lumen diameter was 8.387 ± 2.944 μm in hBVOs of the ND-hydrogel group, whereas it was 40.17 ± 15.76 μm in the D-hydrogel group (Figure 2f). Our findings align with the typical diameter ranges of 5–10 μm for capillaries and 10–100 μm for arterioles, respectively.[23]

The actin cytoskeleton and filopodia of the cells in the vascular organoids were visualized by staining the entire gel with FITC-phalloidin on day 11 (**Figure 3**a). According to bright-field analysis, the vascular organoids within the D-hydrogel exhibited greater numbers of branches than those in the ND-hydrogel group. Two adjacent hBVOs were analyzed with AngioTool to assess hBVO complexity. The results showed that the vascular organoids in the D-hydrogel showed significant increases in explant area, vessel area, total vessel length, and junction number (Figure 3b). These results demonstrated the superior ability of the dynamic matrix to support and promote vascular development in hBVOs.

For a detailed depiction of angiogenesis within the vascular organoids, hBVOs were co-stained with the EC marker CD31 and phalloidin to show the ECs inside the hBVO (Figure 3c). 3D reconstruction of the organoids was performed using Imaris. The 3D structure of the EC membrane, overall cytoskeleton, and nuclei were reconstructed and labeled with dim red, green, and blue (Figure 3d). Two adjacent vascular organoids were pseudo-labeled with different colors, and the cell nuclei were visualized as blue dots (Figure 3e). This allowed for a more comprehensive visualization and analysis of the vascular network within the organoids. EC connections between neighboring organoids were observed in the D-hydrogel group (Figure 3e, white arrows; Videos S1,S2, Supporting Information). This indicates that the dynamic matrix not only provides a more conducive environment for vascular development within individual organoids but also facilitates the formation of connections between multiple organoids, potentially leading to the formation of a larger, more interconnected vascular network.

2.3. Viscoelasticity-Mediated Modulation of Mural Cell Phenotype and Arteriolar Differentiation

To explore the cellular diversity and molecular signature of vascular organoids enclosed in ND- and D-hydrogels, we conducted single-cell RNA sequencing (scRNA-seq) of hBVOs on day 11. A total of 25 558 cells from the ND- and D-hydrogel group were visualized in the uniform manifold approximation and projection (UMAP) (**Figure 4**a). The cells in the vascular organoids can be assigned to six main cell clusters (Figure 4b) using known marker genes: MSCs (7062 cells, 27.6%, marked with *THY1* and *ITGB1*);[24,25] ECs (5544 cells, 21.7%, marked with *CLDN5*); pericytes (PCs) (4251 cells, 16.6%, marked with *NDUFA4L2*);[26,27] SMCs (3261 cells, 12.8%, marked with *TAGLN* and *MYL9*); fibroblasts (FBs) (4441 cells, 17.4%, marked with *COL1A1*)[28,29] and transitional cells (TCs) (999 cells, 3.9%). Both the groups contained MSCs, ECs, and TCs. The composition of the MCs differed between the two groups, with PCs forming in the ND-hydrogel and SMCs forming in the D-hydrogel (Figure 4c). Furthermore, we identified the hBVO cells as belonging to 17 cell types (Figure 4d,e): MSC 1 (2915 cells, 11.4%); MSC 2 (1309 cells, 5.1%); MSC 3 (2838 cells, 11.1%); EC 1 (2397 cells, 9.4%); EC 2 (800 cells, 3.1%); EC 3 (2200 cells, 8.6%); EC 4 (147 cells, 0.6%); PC 1 (2834 cells, 11.1%); PC 2 (118 cells, 0.5%); PC 3 (1299 cells, 5.1%); SMC 1 (681 cells, 2.7%); SMC 2 (1611 cells, 6.3%); SMC 3 (969 cells, 3.8%); FB (4441 cells, 17.4%); TC 1 (279 cells, 1.1%); TC 2 (121 cells, 0.5%) and TC 3 (599 cells, 2.3%). Marker genes and differentially expressed genes (DEGs) confirmed the accuracy of the cell identities (Figure 4f; Figure S7, Supporting Information). In comparison to hBVOs embedded in traditional Matrigel–Collagen I, scRNA-seq was also performed on cells in vascular organoids sprouted in Matrigel–Collagen I on day 11. In our experiment, hBVOs differentiated into MSCs, ECs, epithelial cells, TCs, and an undefined cluster. However, hBVOs in Matrigel–Collagen I consisted of a small proportion of ECs without PC or SMC (Figure S8, Supporting Information).

PC and SMC are two types of cell continuum within MC,[30] and there is currently no consensus on criteria for pericyte identification.[31,32] To address this, the expression of various MC genes was detected in the PC and SMC cell clusters of hBVOs (Figure S9, Supporting Information). *Ndufa4l2* showed predominant expression in the PCs in hBVOs, while *Acta2* and *Tagln* were mainly expressed in SMCs. Moreover, *Rgs5* and *Myl9* were expressed in both cell clusters. To investigate the distribution of ECs, PCs, and SMCs within the hBVOs in the ND- and D-hydrogel, we stained the hBVOs using selected markers. NDUFA4L2+ cells were observed surrounding the CD31+ vessel lumens in the ND-hydrogel group (Figure 4g, white arrowheads), while cells co-stained for α-SMA/ SM22α (proteins for *ACTA2* and *TAGLN*, respectively) were aligned along the CD31+ endothelial lumens in the D-hydrogel group (Figure 4h, white arrows).

To better understand the changes in cell origins and development within vascular organoids, especially the variance between the ND-hydrogel group and D-hydrogel groups, we employed Slingshot to infer hBVO cell trajectory. The analysis yielded a predominantly linear trajectory, with EC, PC, and SMC lineages originating from MSC populations (**Figure 5**a). The ND-hydrogel group consisted of two EC lineages and one PC lineage, whereas the D-hydrogel group consisted of three EC lineages and one SMC lineage. Additionally, in the Monocle analysis, the MSC population was set as the root of the developmental trajectory to illustrate the continuum of cell development in vascular organoids. The developmental trajectory indicated that MSC primarily gave rise to two mature cell types, ECs, and PCs, with SMCs positioned in the middle of the trajectory (Figure 5b). The distribution of the 17 cell types in the developmental trajectory is shown in Figure S10 (Supporting Information). Within the ND-hydrogel, MSCs differentiated into both EC and PC fates, whereas in the D-hydrogel group, MSCs differentiated only into EC fates. To gain insight into how gene expression profiles changed across different cell populations during pseudotime, we constructed a gene expression heatmap in a branch-dependent manner (Figure 5c). As pseudotime progressed, the

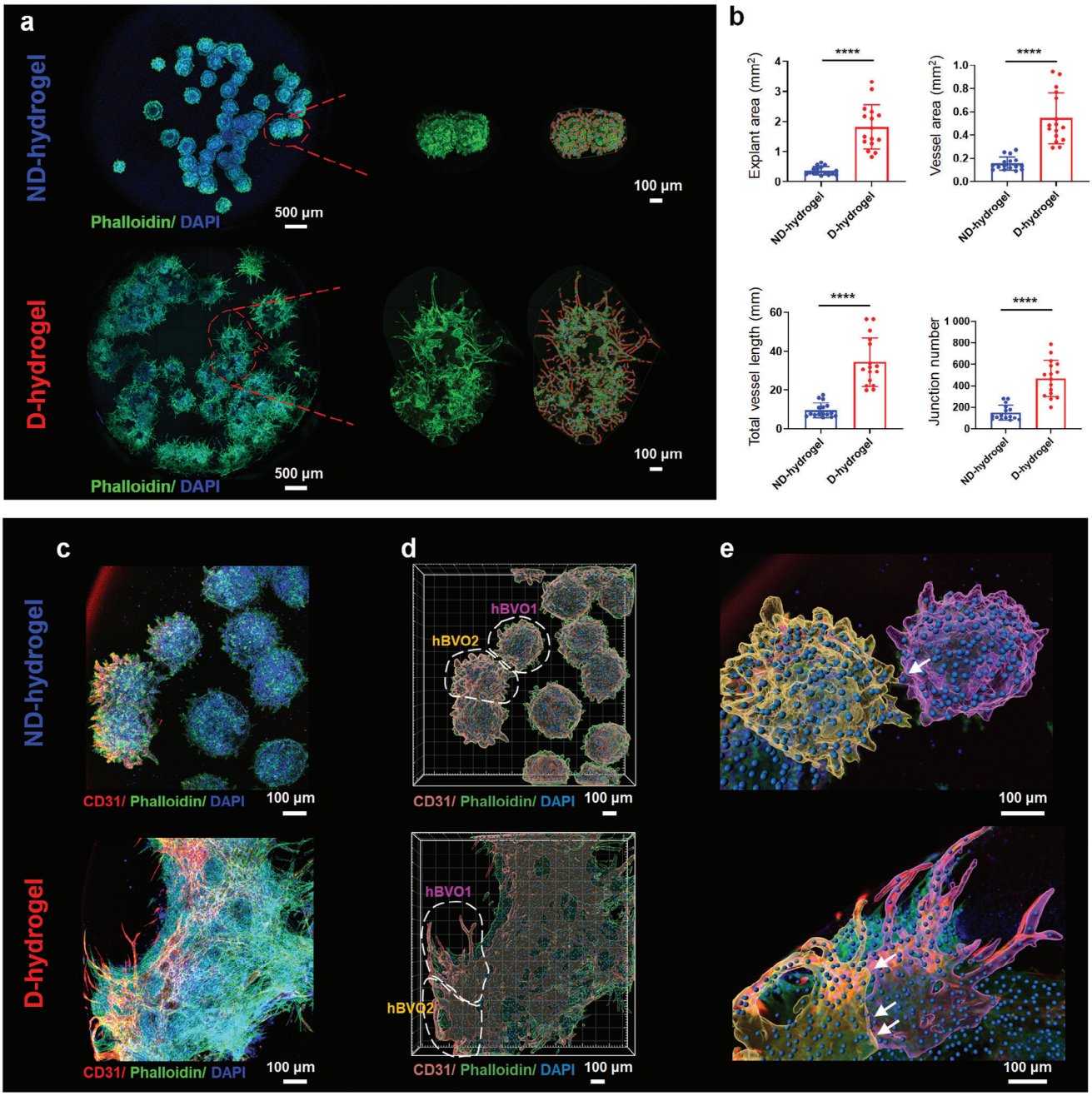

Figure 3. Complexity and angiogenesis of hBVOs in ND- and D-hydrogels. a) Confocal maximum intensity projection images of phalloidin staining of the vascular organoids embedded in the in ND- and D-hydrogels after 5 days in culture. The neighboring vascular organoids were outlined with red dashed lines and their angiogenesis levels were analyzed with AngioTool. Scale bar, 500 μm (left panels), 100 μm (right panel). b) Quantitative analysis of explant area, vessel area, total vessel length, and junction numbers of the vascular organoids from ND- and D-hydrogel groups. ($n = 16$). c) Representative confocal maximum intensity projection images of hBVOs co-stained with CD31, Phalloidin, and DAPI. d) The 3D reconstructions of the vascular organoids in the hydrogels. e) Magnification of adjacent hBVOs outlined in (d) to show anastomosis (white arrows). Scale bar, 100 μm. **** $p < 0.0001$.

expression of the EC marker genes *CDH5, CLDN5,* and *PECAM1* increased in the EC fate branch in both the ND- and D-hydrogel groups, as expected (Figure 5d–f). The pericyte marker gene *NDUFA4L2* showed increased expression in the PC fate branch in the ND-hydrogel group, while no expression of *NDUFA4L2* was detected in hBVOs embedded in D-hydrogel (Figure 5g). Surprisingly, the SMC marker gene *MYL9* was upregulated at the initiation of both cell fate branches (Figure 5h). In contrast to the expression pattern of *NDUFA4L2, MYL9* was mainly expressed in both cell fates in the D-hydrogel group, with only a few expressions at the beginning of the PC fate in the ND-hydrogel group.

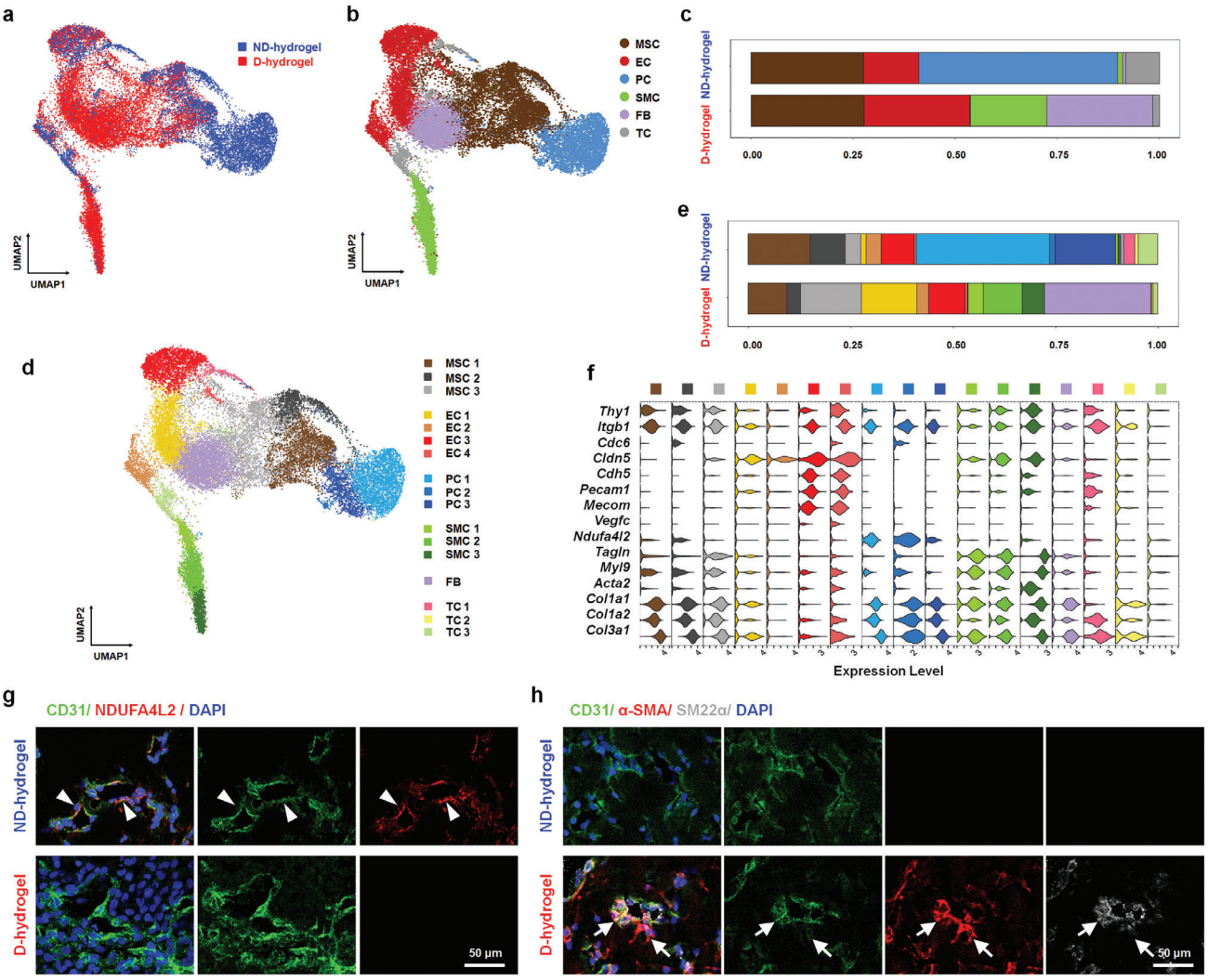

Figure 4. Single-cell RNA sequencing identified different cell clusters in vascular organoids sprouted in ND- or D-hydrogels. a) UMAP visualization of 25 558 cells obtained from vascular organoids in ND-hydrogel (blue) and D-hydrogel (red). b) UMAP of vascular organoid cells colored by 6 main cell clusters. MSC, mesenchymal stem-like cell; EC, endothelial cell; PC, pericyte; SMC, smooth muscle cell; FB, fibroblast; TC, transitional cell. c) Bar graph of the proportion of six main captured cell clusters in hBVOs from ND- and D-hydrogels. d) UMAP of vascular organoid cells colored by 17 cell types. e) Bar graph of the proportion of 17 captured cell types in hBVOs from ND- and D-hydrogels. f) Violin plots showing marker genes for 17 distinct cell types. A violin plot was drawn to show the expression levels of the marker genes in the 17 cell clusters. g,h) Immunostaining of markers of CD31 with NDUFA4L2, α-SMA, and SM22α in hBVOs embedded in ND- or D-hydrogels. Scale bar, 50 μm.

2.4. Molecular Mechanisms Underlying the Regulation of Matrix Viscoelasticity on hBVO Development

To explore the mechanism underlying how viscoelasticity regulates the development of vascular organoids, we compared gene expression between the ND- and D-hydrogel groups in MSCs, ECs (Figure S11, Supporting Information), and MCs (PCs + SMCs) (Figure S12a, Supporting Information). Then, the enrichment of gene ontology (GO) terms for the DEGs was calculated. It indicated that the difference between hBVOs in the ND- and D-hydrogels was related with functional processes such as "cell adhesion molecular binding," "cell-substrate adherens junction," "focal adhesion," and "cadherin adhesion" in MSC, EC, and MC cell populations (**Figure 6**a,b; Figure S12b, Supporting Information). We then focused on integrin subunit genes, as they play crucial roles in cell adhesion and are known to be regulated by changes in matrix properties. *ITGB1* and *ITGA5* were significantly upregulated in the MSC and MC populations in the D-hydrogel group compared to those in the ND-hydrogel group (Figure 6c; Figure S12c, Supporting Information). Notch signaling is known to regulate arterial differentiation during vessel maturation, and we found that notch receptor 3 *(NOTCH3)* was increased in the MSC population in the D-hydrogel group compared with that in the ND-hydrogel group. Additionally, platelet-derived growth factor B (*PDGFB)*, which is secreted by ECs to recruit pericytes during vascular development, showed increased expression in ECs from the ND-hydrogel group compared to those from the D-hydrogel group (Figure 6d).

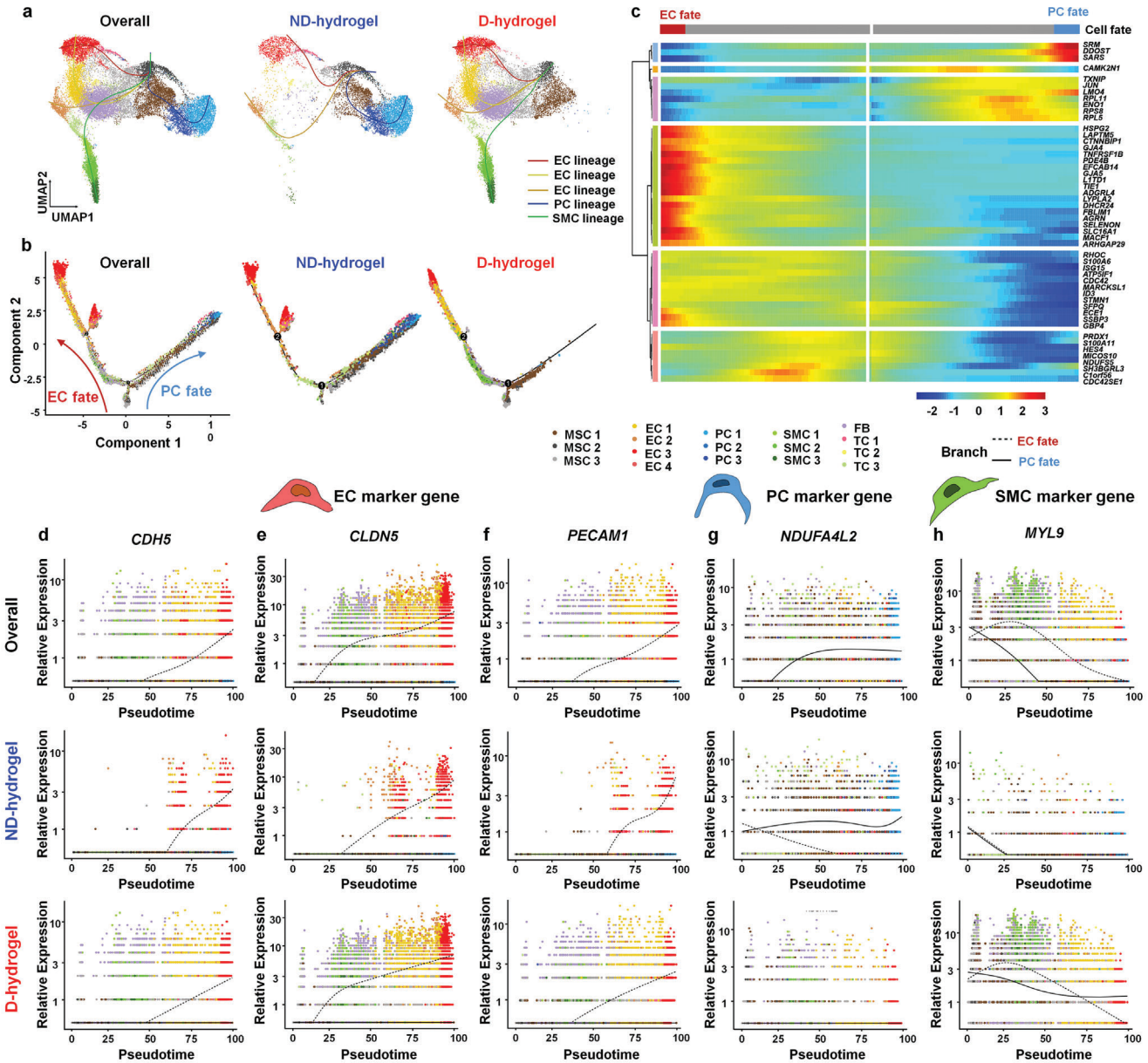

Figure 5. Single-cell trajectory analysis and pseudotime reconstruction of hBVO cell populations. a) Slingshot trajectory analysis of hBVO cells reveals linear trajectories of EC, PC, and SMC lineages originating from MSC populations. b) Monocle pseudotime trajectory branch shows the changing progression from MSCs to ECs or PCs in overall hBVO cells, and the ND- or D-hydrogel groups. c) Branch-dependent expression of genes from the root to EC or PC fate. d–h) Representative EC, PC, or SMC marker genes in EC or PC fate branches ordered by Monocle analysis along pseudotime in overall, ND-hydrogel, and D-hydrogel groups. Cell types along with the developmental trajectory were labeled by different colors.

To validate the two pathways, immunostaining was performed to assess protein expression (Figure S13, Supporting Information). Furthermore, hBVOs embedded in the D-hydrogel were exposed to the γ-secretase inhibitor DAPT and the PDGFRβ inhibitor CP673451 for additional validation. The effect of mechanotransduction signaling was also studied by treating hBVOs in the D-hydrogel with the FAK inhibitor PF562271, as well as the YAP/TAZ inhibitor-1. Treatment with PF562271, YAP/TAZ inhibitor-1, and DAPT led to a decreased area, disorganized structure, and thinning of vessel sprouts, while inhibition of PDGFRβ with CP673451 showed a tendency to form thicker vessel tubes (Figure 6e–g; Figure S14, Supporting Information). These results imply that the regulation of matrix viscoelasticity may affect hBVO development through modulating mechanotransduction and NOTCH3 signaling, as well as PDGFB signaling.

2.5. Cardiac Repair Post-Transplantation of hBVOs with D-Hydrogel in Myocardial Infarction

To assess the impact of in vivo transplantation on the hydrogel, the D-hydrogel was implanted on the backs of mice. The

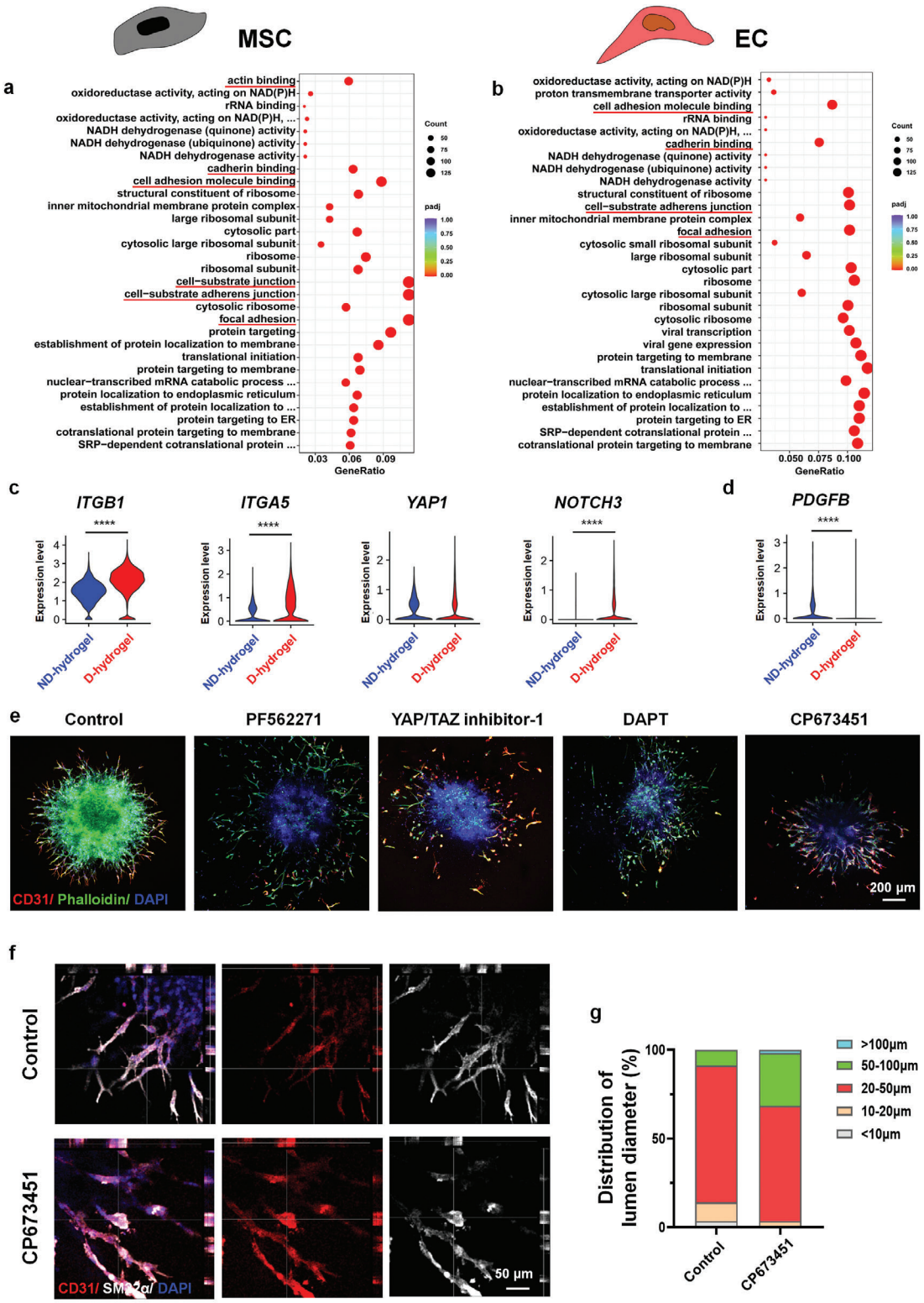

Figure 6. DEG analysis of EC and MSC populations, revealing the molecular differences influenced by matrix viscoelasticity. a,b) GO enrichment analyses for MSC (a) and EC (b) clusters between the ND-hydrogel group and the D-hydrogel group. c,d) Violin plots showing a quantitative comparison of selected genes in MSC (c) and EC (d) clusters between the ND-hydrogel group and D-hydrogel group. e) Representative confocal images of hBVOs embedded in the D-hydrogel after exposure to PF562271, YAP/TAZ inhibitor-1, DAPT, and CP673451. Scale bar, 200 μm. f) Confocal orthogonal section images of hBVO sprouts from the control and CP673451 groups. Scale bar, 50 μm. g) Distribution of the lumen diameter of hBVOs in the D-hydrogel with or without CP673451 ($n = 57$, from three different batches). **** $p < 0.0001$.

D-hydrogel remained post four weeks, and its viscoelasticity persisted after transplantation (Figure S15, Supporting Information).

To investigate whether hBVOs can integrate after transplantation with D-hydrogel, iPSCs genetically labeled with a green fluorescent protein (GFP) were induced into hBVOs. Then the GFP-hBVOs were mixed with D-hydrogel, cross-linked, and transplanted into NOD-SCID mice. After one week, GFP-labeled vessels were found to be connected with the host vessels (Figure S16, Supporting Information).

To test the therapeutic effects of hBVOs and D-hydrogels for MI, an MI model was induced in Sprague–Dawley (SD) rats by ligating the left anterior descending coronary arteries. Following this procedure, PBS, hBVO with ND-hydrogel, or hBVO with D-hydrogel were administered into the ischemic area of the heart through multipoint injections. Four weeks post-injection, echocardiography was performed to evaluate the therapeutic effects of the grafts on cardiac function in MI rats (**Figure** 7a). The hBVO + D-hydrogel groups exhibited improvements in ejection fraction (EF) and fractional shortening (FS), along with a decrease in left ventricular diastolic diameter (LVIDd) and left ventricular systolic diameter (LVIDs), compared to the PBS group. Furthermore, the hBVO + D-hydrogel group displayed better cardiac function than the hBVO + ND-hydrogel group (Figure 7b). HE and Masson staining were conducted 4 weeks post-MI to assess the structure and fibrosis of the heart (Figure 7c,d). Both ND- and D-hydrogel-encapsulated hBVO showed reductions in cardiac fibrosis compared with the PBS group. Meanwhile, the hBVO + D-hydrogel group displayed greater alleviation of cardiac fibrosis than the hBVO + ND-hydrogel group (Figure 7e). These results suggest that transplantation of hBVOs with D-hydrogel can effectively improve cardiac function and reduce fibrosis in an MI model.

To investigate the differentiation of capillaries and arterioles in vivo, immunohistochemical staining of heart samples was performed 4 weeks after MI. The capillaries and arterioles were distinguished using the EC marker CD31 with SMC markers α-SMA and SM22α (**Figure** 8a). Compared with the PBS group, no significant differences were observed in the capillary density of the infarcted zone (IZ) of the ischemic heart in the hBVO + ND- or hBVO + D-hydrogel groups (Figure 8b). Interestingly, the combination of hBVO with the D-hydrogel significantly increased the arteriole density in the IZ of the ischemic area compared to the PBS or hBVO + ND-hydrogel groups (Figure 8c). This suggests that, when encapsulated in the D-hydrogel, the injected hBVOs exhibited a greater tendency to differentiate into arterioles. Consistent with the in vitro findings, these results indicate that hBVOs encapsulated in the D-hydrogel have greater potential for neovascularization in vivo.

3. Discussion

In this study, we present a tissue engineering strategy for the rapid generation of human arteriole-like structures using hPSCs and a synthetic dynamic hydrogel. Our method investigated the influence of the viscoelastic properties of a matrix on self-organization and multipotent differentiation during the development of vascular organoids. When encapsulated within a dynamic hydrogel, vascular organoids form arterioles comprising ECs, SMCs, FBs, and MSCs. Moreover, they demonstrated an ability to adapt to arterial reconstitution post-MI in vivo. With a completion time of only 11 days, this method is robust and suitable for mass production, demonstrating considerable potential for clinical translation in the regeneration and repair of ischemic tissues.

Gerecht et al. have conducted a series of studies on how dynamic hydrogel networks regulate vasculogenesis and angiogenesis. Using endothelial colony-forming cells (hECFCs) as a model, they discovered that a D-hydrogel increased microvessel formation and angiogenesis in hECFCs through integrin signaling in vivo.[33] Recently, they synthesized a collagen–hyaluronic acid-based hydrogel with tunable plasticity as a dynamic and covalent network. Interestingly, during EC vasculature formation, the hydrogel with medium plasticity showed the largest tubular lumen and longest invading distance.[34] The vascular system comprises a range of cells, primarily ECs, that line the inner surface of blood vessels as well as adjacent vascular MCs, including SMCs and PCs.[35] Consequently, relying solely on ECFCs or ECs is not sufficient to capture cell heterogeneity in blood vessels, especially in terms of pericyte recruitment and EC-MC crosstalk during vessel maturation.[36]

Blood vessel organoids were formed by initiating a common pool of mesodermal progenitors and then differentiating into various vascular cell types. These organoids replicate the intrinsic self-organization of vascular cells during their development. The mature hBVOs that sprouted on collagen I-Matrigel gels were identified as capillary organoids because of their composition of ECs, PCs, and MSCs.[11] In a preprint report, Nikolova et al. conducted a comprehensive single-cell transcriptomic analysis of hBVOs at different stages, revealing a bifurcation in endothelial and mural fate during organoid development.[37] The shortcomings of the current organoid protocol include the inability to induce vascular SMCs and generate larger vessels.[14] Aligned with the above reports, our study showed similar cell compositions of hBVOs in the ND-hydrogel. Unexpectedly, the MCs differentiated into SMCs instead of PC in a dynamic matrix network of hBVOs.

The native vascular hierarchy includes the arteries, arterioles, capillaries, venules, and veins. The differentiation between arteries and veins is vital for establishing a properly functioning circulatory system. During the bifurcation between artery and vein ECs, TGF-β and Notch signaling specify artery fate, whereas PI3K instructs vein identity.[38] The activation of the Notch pathway is essential for determining arterial identity, relying on interactions between cell surface receptors and ligands.[39] As a transmembrane protein, Notch triggers its receptor through direct contact with neighboring cells. Upon ligand binding, the Notch receptor is cleaved, leading to the translocation of the Notch intracellular domain into the nucleus, where it activates downstream arterial-specific genes.[40] During pericyte recruitment, PDGFB is secreted by ECs in angiogenic sprouts and serves as an attractant for comigrating PCs.[41] Our research revealed that *NOTCH3* was upregulated in MSC within the vascular organoids encapsulated in the D-hydrogel network, whereas *PDGFB* was diminished in the EC population. This may provide an environment for arteriolar differentiation. These results suggest that the viscoelastic matrix may provide a suitable microenvironment for the effective

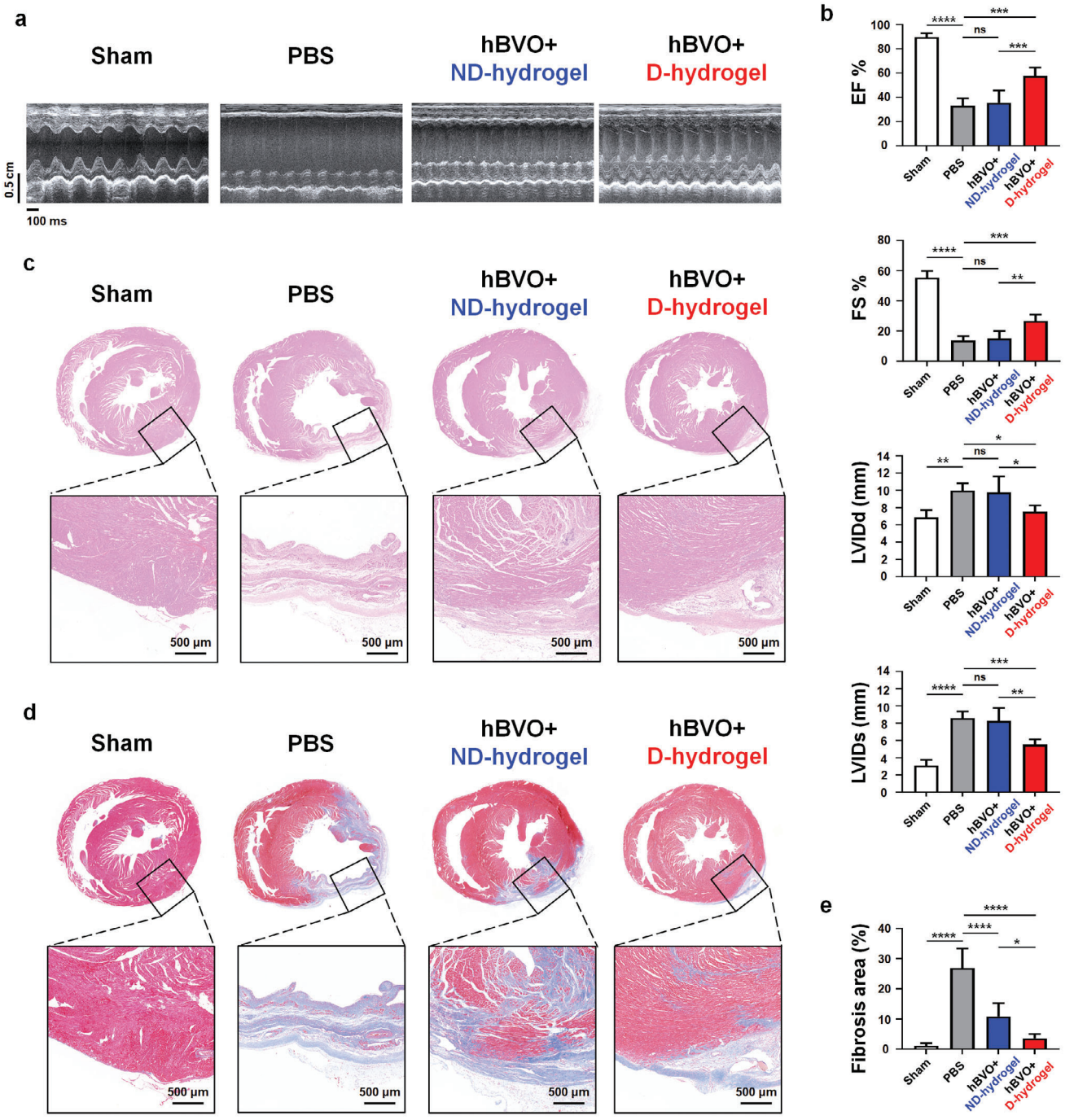

Figure 7. The combination of hBVOs and D-hydrogel ameliorates cardiac dysfunction in myocardial infarction (MI). a) Representative echocardiogram depicting cardiac function of rats in different treatment groups 4 weeks post-MI. b) The statistical results for ejection fraction (EF), fractional shortening (FS), left ventricular diastolic diameter (LVIDd), and left ventricular systolic diameter (LVIDs) based on echocardiographic data. ($n = 5$ for each group). c,d) Hematoxylin-eosin and Masson staining showing the structural changes and fibrosis in the rat hearts. e) A quantitative analysis of the extent of fibrosis in the hearts. ($n = 5$ for each group). * $p < 0.05$, ** $p < 0.01$, *** $p < 0.001$, **** $p < 0.0001$, and ns, not significant.

specification of vascular cells, leading to the formation of arteriolar structures in vivo.

The generation of collateral arteries is advantageous in aiding the rehabilitation of ischemic vascular conditions. In the case of neonatal heart injury, ECs migrate from arteries along existing capillaries and reassemble into collateral arteries. However, this arterial reassembly process is nearly absent in adults.[42] Through an ingenious dual genetic system, capillary ECs have been traced and found to contribute to collateral arteries in the neonatal heart. However, capillary ECs have been found to contribute to arterial

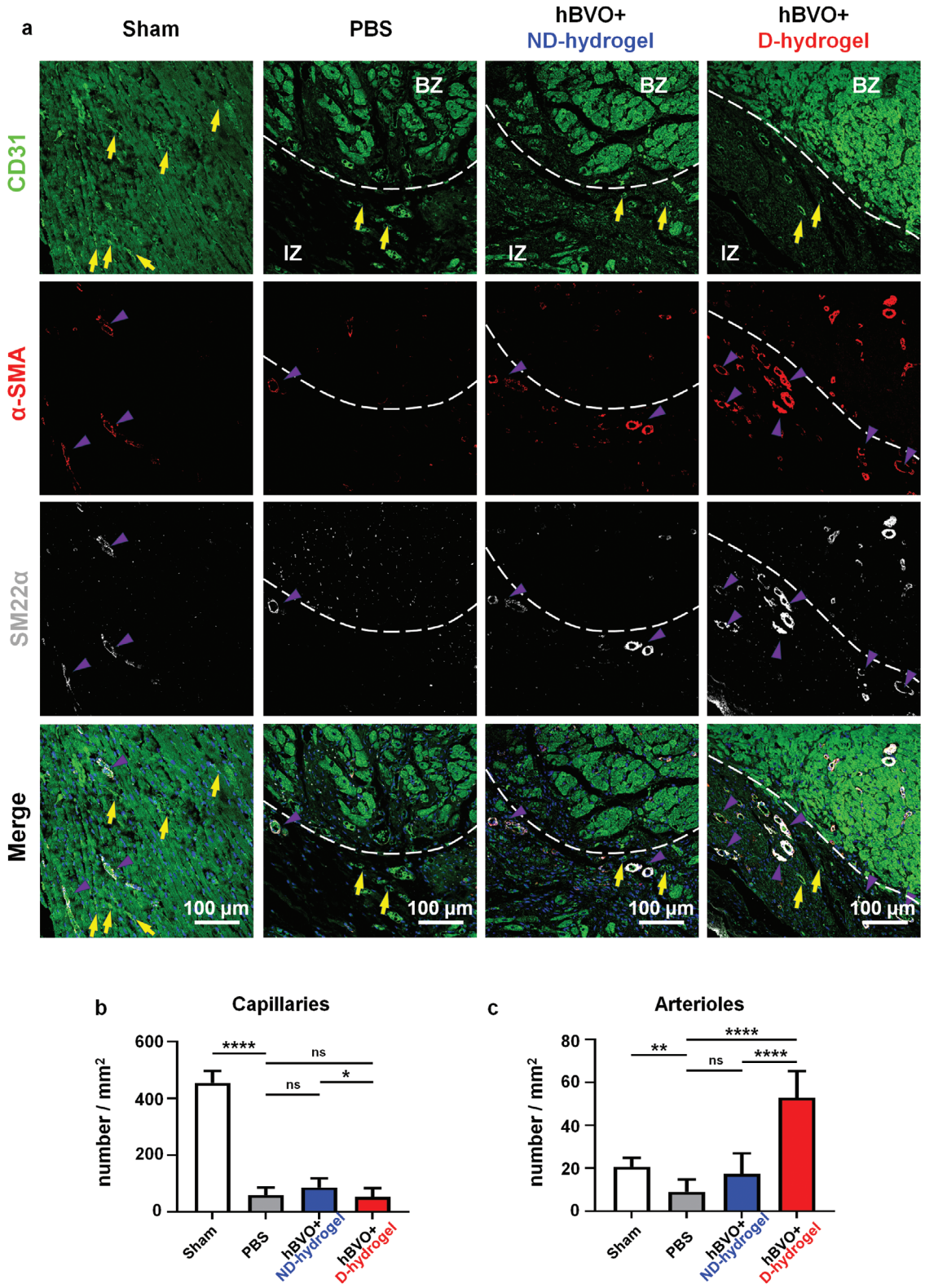

Figure 8. The combination of hBVOs and D-hydrogel promotes angiogenesis and arteriole differentiation in MI hearts. a) Representative images of fluorescence immunostaining for CD31, alpha-smooth muscle actin (α-SMA), and SM22α in rat hearts at 4 weeks post-MI. b,c) Quantitative analysis of capillary density (CD31+) and arteriole density (α-SMA+/SM22α+) in the infarcted zone of ischemic hearts. Arteriole density was determined by counting vascular structures that co-expressed α-SMA and SM22α (violet arrowheads). Vessels that solely expressed CD31 were identified as capillaries (yellow arrows). (n = 15 for each group). BZ, border zone; IZ, infarcted zone. * $p < 0.05$, ** $p < 0.01$, **** $p < 0.0001$, and ns, not significant.

ECs in adult hearts only after severe MI.[43] In our study, the hBVOs formed within the D-hydrogel differentiated into arteriole-like structures after MI, which may have contributed to arterial reassembly and neovascularization in the ischemic area. Nevertheless, further detailed spatio-temporal tracking is required for the development process of SMCs in vascular organoids, and additional investigation is needed to comprehend the balance of mural cell differentiation between SMCs and PCs. Moreover, the hBVOs within dynamic hydrogels seem to develop layered structures, possibly due to the organoids settling during prolonged gelation periods. This aspect could be further investigated in future studies to optimize the hydrogel conditions for enhanced vascular organization and functionality.

4. Conclusion

In conclusion, our study describes a strategy for generating hBVO-derived human arterioles with SMCs by regulating matrix viscoelasticity. By synthesizing a dynamic matrix, we observed an increase in focal adhesions in MSCs and MCs during the development of vascular organoids, creating a conducive environment with heightened NOTCH3 levels and reduced PDGFB expression in EC to facilitate vascular organization and arteriole differentiation. When transplanted in vivo, the combination of hBVOs and a dynamic hydrogel effectively promoted the reassembly of arterioles and repaired cardiac function in the infarcted heart. This study emphasized the significance of integrating matrix viscoelastic properties into biomaterial design to create functional and complex vascular networks for tissue engineering. The formation of arterioles is crucial for effectively incorporating hBVOs into larger tissue constructs and holds great promise for translational applications in regenerative medicine.

5. Experimental Section

Materials: NaOH, NaCl, β-cyclodextrin (β-CD), *N, N*-dimethylformamide, and acryloyl chloride were obtained from J&K Scientific (Beijing, China). Dimethyl sulfoxide, hydrochloric acid, and deuterium oxide were purchased from Energy Chemicals. Triethylamine was obtained from Macklin (Shanghai, China). Gelatin was obtained from Sigma-Aldrich (St. Louis, MO, USA). Methacrylic anhydride and lithium phenyl (2,4,6-trimethylbenzoyl) phosphinate (LAP) were obtained from TCI (Tokyo, Japan).

Synthesis of Ac-β-CD: First, 10 g β-CD was mixed in 150 mL of DMF with 7 mL of TEA. The mixture was stirred and cooled to 0 °C, and then 5 mL of acryloyl chloride was dripped into the solution slowly over 1 h. After stirring for 6 h, the mixture was filtered and concentrated to ≈20 mL using a vacuum rotary evaporator. The concentrated solution was dropped into acetone (600 mL) to obtain a white precipitate, which was then washed twice with acetone and vacuum dried for 3 days.

Synthesis of GelMA: Five grams of gelatin was added into 50 mL of distilled (DI) water and fully dissolved at 50 °C for 30 min to prepare a 10% gelatin solution. Then, 0.5% v/v methyl acrylate was added, and the mixture was stirred for 3 h at 50 °C. Subsequently, the solution was dialyzed in DI water at 45 °C for 7 days, and the DI water was changed thrice daily. Finally, GelMA was obtained by lyophilization.

Synthesis and Fabrication of Hydrogels: To prepare the GelCD hydrogel, gelatin (80 mg) and Ac-β-CD (100 mg) were dissolved in 900 µL of PBS buffer (1×) overnight at 37 °C. Then, 100 µL of LAP (wt = 5%) was added to this mixture at 37 °C. After cooling to room temperature, the mixture was exposed to blue light (6 W, 405 nm) for 5 min to obtain a GelCD hydrogel. The preparation of GelMA hydrogel: GelMA (80 mg) was dissolved in 900 µL of PBS buffer (1×) to obtain 8% GelMA solution, and then 100 µL of the aforementioned photoinitiator was added. The mixture was irradiated with blue light for 5 min to obtain the GelMA hydrogel.

Characterization of Mechanical Properties: A hybrid rheometer (HR-30; TA Company, New Castle, DE, USA) was used to evaluate the rheological properties of the hydrogels. Hydrogels were prepared as circular slices with a diameter of 8 mm and a volume of 150 µL. Oscillating strain–sweep experiments were conducted to determine the linear viscoelastic regions of the hydrogels. These experiments were performed at a constant frequency of $\omega = 10$ rad s^{-1} involved dynamic strain scan tests ranging from 1% to 400%. Subsequently, the frequency was set to 10 rad s^{-1}, and the hydrogels were maintained at 1% shear strain for 180 s to evaluate the storage and loss moduli. Subsequently, a frequency sweep (1–63 rad s^{-1}) was performed at 1% strain, followed by a frequency fixation at 10 rad s^{-1}, and the sample was held at 1% shear strain for 40 s. The shear strain was then increased to 1000% and maintained for 40 s. This alternating shear strain process was repeated thrice to observe the self-healing properties of the hydrogels. Compression experiments were performed to test the stress–relaxation properties of the hydrogels. The samples were compressed to a strain of 15% at a deformation rate of 0.3 mm s^{-1} at 37 °C.

Human iPS Cell Culture and hBVO Differentiation: The DYR0100 human iPSC line (SCSP-1301) was obtained from the Cell Bank of the Chinese Academy of Sciences. The iPS cells (passages 10 to 30) were cultured on Matrigel (Corning, NY, USA) in mTeSR1 medium (STEMCELL Technologies, Vancouver, BC, Canada) under feeder-free conditions and tested for mycoplasma contamination on a regular basis. HBVO differentiation was performed using a modified version of a previously described method.[12] Briefly, the iPS cells were dissociated using 0.5 mM EDTA for 3 min and Accutase (STEMCELL Technologies) for 3 min. Then, 1.5×10^5 cells were resuspended in an aggregation medium with 50 µM Y-27632 (BioGems, Westlake Village, CA, USA). The aggregation medium constituted of KnockOut DMEM/F12 (Gibco, Waltham, MA, USA) with KnockOut Serum Replacement (Gibco), Glutamax (Gibco), NEAAs (Gibco) and β-mercaptoethanol (Sigma). The cells were plated into one well of AggreWell800 (STEMCELL Technologies) for cell aggregation. Cell aggregates were treated on day 1 with 12 µM CHIR99021 (BioGems) and 30 ng mL^{-1} BMP4 (PeproTech, Cranbury, NJ, USA) in N2B27-medium for mesoderm induction, and on day 4 with 100 ng mL^{-1} VEGF-A (PeproTech) and 2 µM Forskolin (Sigma) in N2B27-medium for vascular lineage induction.

Embedding Organoids into the Gel: On day 6, the organoids were transferred from the AggreWell and settled in centrifuge tubes by gravity. The medium was carefully removed from the tubes and the previously prepared GelCD/GelMA solution with LAP was added. Blood vessel organoids were encapsulated in the hydrogel at a concentration of ≈50 organoids per 50 µL hydrogel. The mixture was then exposed to 405 nm blue light for 5 min to crosslink the hydrogel. The organoid-laden hydrogels were cultivated in StemPro-34 complete medium (Gibco) containing 100 ng mL^{-1} VEGF-A, 100 ng mL^{-1} FGF-2 (Peprotech), and 15% FBS (Gibco) for 5 days to induce vascular network sprouting.

Cell Viability Analysis: Cell viability was evaluated using a calcein-AM/PI live/dead kit (PF00007; Proteintech, Wuhan, China) under different conditions, including extrusion with 200 µL pipette tips, blue light crosslinking post-extrusion from tips, extrusion with a 30G needle, and blue light crosslinking after needle extrusion. Briefly, hBVOs were suspended in D-hydrogel and treated under the aforementioned conditions on day 6. After culture, hBVOs were rinsed twice with warm DPBS and incubated for 30 min in DPBS with 2 µM calcein-AM and 4.5 µM PI. Subsequently, the hBVOs were washed twice with warm DPBS and visualized using a confocal microscope.

In vitro Inhibitor Assay: To inhibit γ-secretase, DAPT (25 µM; HY-13027; MCE, New Jersey, NJ, USA) was utilized, while CP-673451 (1 µM; S1536; Selleck, Texas, TX, USA) was added to the medium to inhibit PDGFRβ. PF-562271 (1 µM; HY-10459; MCE) and YAP/TAZ inhibitor-1 (1 µM; HY-111429; MCE) were employed to inhibit the FAK and YAP pathways, respectively. During the vessel sprouting stage, the hBVOs embedded in the D-hydrogel were exposed to the above inhibitors.

Immunofluorescence: For whole-mount immunofluorescence staining, the organoid vascular networks in the D-hydrogel- or ND-hydrogel were directly fixed for 20 min with 4% (v/v) paraformaldehyde at room temperature and blocked with an immunostaining blocking/primary antibody dilution solution (Beyotime, Beijing, China) for 2 h at room temperature on a shaker. For paraffin sections, the gels were dehydrated and embedded in paraffin. Paraffin samples were cut into sections of 5 µm using a microtome. Paraffin sections were deparaffinized in xylene, rehydrated using graded alcohol, and processed for antigen retrieval by boiling in 10 mM citrate buffer (pH 6.0) for 2 min. To block nonspecific binding, sections were incubated with an immunostaining blocking/primary antibody dilution solution (Beyotime) for 30 min at room temperature. The whole mount samples or paraffin sections were then incubated with primary antibodies overnight at 4 °C. The following antibodies and reagents were used in this study: anti-human CD31 (ab281583, 1:400; Abcam, Cambridge, UK), anti-human CD31 (BBA7, 1:400; R&D, Minnesota, MN, USA), anti-Claudin 5 (PA5-99415, 1:200; Thermo Fisher Scientific, Waltham, MA, USA), anti-NDUFA4L2 (GTX66244, 1:200; GeneTex), anti-α-SMA (A2547, 1:200; Sigma), anti-α-SMA (ab124964, 1:200; Abcam), anti-SM22α (ab10135, 1:200; abcam), anti-THY1 (ab181469, 1:500; Abcam), anti-Integrin B1 (ab179471, 1:1000; Abcam), anti-Integrin A5 (ab150361, 1:400; Abcam), anti-NOTCH3 (ab315348, 1:500; Abcam) and anti-PDGFB (ab107101, 1:200; Abcam). To stain the cytoskeleton, samples were incubated with Alex Fluor 488 Phalloidin (A12379, 1:400; Invitrogen, Waltham, MA, USA) for 20 min at 4 °C. After three 10-min washes in PBST, the samples were incubated with the corresponding secondary antibodies (1:200 dilution) for 2 h at room temperature. The samples were then counterstained with DAPI and mounted with a fluorescence mounting medium (sc-24941; Santa Cruz Biotechnology, Dallas, TX, USA).

Transmission Electron Microscopy: TEM was performed as previously described.[44] Briefly, after vascular sprouting in the gel for 5 days, the whole-mount gel was cut into small fragments using syringe needles. The gel samples were fixed in 3% glutaraldehyde, postfixed in 1% osmium tetroxide, dehydrated in an ascending series of acetone and propylene oxide, and embedded in epoxy resin 618. Ultrathin sections were observed under a transmission electron microscope (HT7800; Hitachi, Tokyo, Japan) at an operating voltage of 120.0 kV with magnification as indicated in the figures.

Image Acquisition, Analysis, and 3D Reconstruction: Brightfield images of hBVOs were captured with a Leica DM IL LED Microscope (Leica, Wetzlar, Germany) on days 7, 9, and 11. The area and maximum length of the overall hBVOs were measured and normalized with day 7 as the baseline at 100%. For confocal images of vascular lumens of hBVOs, the lumen circumference (p) was measured and used to calculate the diameter (d) by applying the formula $d = p/\pi$. Z-stack fluorescence images of the vascular networks were taken with a Zeiss 900 Laser Scanning Microscope with 10× or 20× objectives. For whole-mount imaging of the fixed gels, seven stacks with heights of ≈300 µm were acquired and converted into total z-projections using ZEN software (version 2.3 blue edition). The explant area, vessel area, total vessel length, and junction number were quantified using AngioTool software (version 0.6a). For 3D reconstruction, a total of ≈200 consecutive images with an interspace of 1.67 µm and a total volume of 0.497 mm^3 were captured for each microscopic field in the selected ROI. Surface reconstruction of vascular organoids was performed using Imaris software (version 10.0.0).

Single-Cell RNA Sequencing: Vascular organoids embedded in D- or ND-hydrogels were dissociated into single cells on day 11. Each group consisted of ≈150 vascular organoid networks isolated from three independent gels. Briefly, the hydrogels were digested at 37 °C in DPBS solution containing 2 mg mL^{-1} collagenase and 2.5 mM $CaCl_2$ and then minced by pipetting them up and down. Next, the samples were digested twice with TrypLE (Gibco) on a shaker at 37 °C for 5 min. The remaining gel fragments were removed using a 40 µm cell strainer, and cells were centrifuged at 200 g for 5 min. Dissociated cells were kept on ice until further use. The cell suspension was loaded into Chromium microfluidic chips with Next GEM Single Cell 3′v3.1 chemistry and barcoded using a 10× Chromium Controller (10× Genomics, Pleasanton, CA, USA). Subsequently, RNA from the barcoded cells was reverse-transcribed and sequencing libraries were constructed using reagents from a Chromium Next GEM Single Cell 3′ Kit v3.1 (10× Genomics). Sequencing was performed on an Illumina NovaSeq 6000 platform (San Diego, CA, USA) following the manufacturer's instructions.

Quality Control and Cell Filtering: The Raw reads from the sequencing data were processed using the 10× Genomics Cell Ranger pipeline V7.1 with default settings. The demultiplexed reads were mapped to the reference genome, and subsequent single-cell analyses were performed using Cell Ranger and Seurat V4. The cell Ranger count took FASTQ files and performed alignment, filtering, barcode counting, and UMI counting. It used Chromium cellular barcodes to generate feature-barcode matrices, identify clusters, and analyze gene expression. Unique molecular identifiers were counted for each gene and cell barcode to create digital expression matrices. Seurat performed additional filtration steps, considering a gene as expressed if it was detected in more than three cells and required each cell to have at least 200 expressed genes. A total of 25 558 high-quality cells were obtained from the vascular networks after filtering.

Cell Clustering and Differential Gene Expression Analysis: Seurat employed the "LogNormalize" method to standardize the gene expression matrix. This involved dividing the expression of each gene by the overall gene expression in a cell, converting it to relative abundance, multiplying it by a normalization factor (typically 10 000), and then performing a log transformation. Seurat cell subtypes were identified using principal component analysis (PCA). The most significant principal components were evaluated and used for cluster analysis to decrease data dimensionality. The graph-based clustering algorithm generated a k-nearest neighbor graph using the Euclidean distance and applied the Louvain algorithm to group cells and optimized the modules. Based on the clustering results, a UMAP dimensionality reduction algorithm was employed to display the cell distribution in a 2D space. To identify differentially expressed genes among the different cell clusters, Seurat was used to compare each cluster with the others. The Wilcoxon rank-sum test was used to identify DEGs in each cluster. Cell types were annotated using previously published marker genes.[25,28,29] The top 10 differential genes identified in each cluster (sorted by $\log_{FC}$) were shown in the overall heatmap.

Slingshot and Monocle Trajectory Analysis: Slingshot (v2.2.0)[45] was used to infer differentiating trajectories within the cell clusters of vascular organoids. The Seurat analysis results (UMAP dimension reduction) were converted to a "SingleCellExperiment." Trajectory inference was conducted using the slingshot function by specifying MSCs as the starting position. Subsequently, the "GetLineages" and "GetCurves" functions were applied to perform trace inference on the cluster based on the minimum spanning tree, and the main curve of the smooth branching path was calculated. The Monocle 2R package (v 2.18.0)[46] was used to generate pseudo-time trajectories for cells within the hBVOs. The clustered cells were input into Monocle to infer the developmental relationships among the vascular organoid cell clusters. Through unsupervised analysis, Monocle's "dispersion table" algorithm was employed to identify genes with high dispersion. These genes were then used to generate developmental trajectories and heatmaps. Mesenchymal stem-like cells were inferred as the starting point of the pseudotime. The "plot_genes_in_pseudotime" function was employed with the top three genes to fit the curve and visualize the gene trend over pseudotime.

GO Enrichment Analysis: To investigate the biological processes and signaling pathways associated with different hydrogel treatments or various cell clusters (subtypes), GO analysis was performed with the "ClusterProfiler" R package (v4.0.5). Pathways with a P value < 0.05 were considered significantly enriched. The significant pathways were visualized as dot plots.

Animal MI Model and Treatment: Eight-week-old male Sprague–Dawley rats were acquired from the Laboratory Animal Center of the Army Medical University. All rats were housed in a temperature-controlled room with a 12-h light: dark cycle, with food and water available ad libitum. All animal experiments were approved by the Laboratory Animal Welfare and Ethics Committee of the Army Medical University (AMUWEC20230154). For MI surgery, the rats were anesthetized by inhalation of isoflurane (2.5% (v/v)), followed by subcutaneous meloxicam administration (5 mg kg^{-1}), and their breathing was sustained using a ventilator. The left anterior

descending coronary artery was ligated using a 6-0 nylon suture. The MI models were randomly divided into the following four groups ($n = 5$ per group): 1) Sham, 2) PBS, 3) hBVO + ND-hydrogel, and 4) hBVO + D-hydrogel. A total of 50 hBVOs were suspended in 50 µL of ND- or D-hydrogel and injected into the border region of the infarct area using 30G needles at three sites in the myocardium. Rats were administered cyclosporine A (10 mg kg^{-1} d^{-1}, Neocyspin) daily until study completion. Four weeks post-injection, the rats were sacrificed via CO_2 overdose. The hearts were collected, washed with heparinized saline, and then fixed with 4% paraformaldehyde.

In vivo Vascular Network–Forming Assay: Five-week-old male NOD-SCID mice were obtained from Hunan SJA Laboratory Animal Co., Ltd. On day 6, hBVOs were suspended in 200 µL D-hydrogel and placed into a 48-well plate. They were then exposed to blue LED light (405 nm) for 5 min to cross-link the hydrogel. Each hydrogel contained 200 hBVOs. After anesthesia, a small incision was made on the back of the mice to create a subcutaneous pocket between the skin and muscle. The hydrogels containing hBVOs were inserted and the incision was closed with sutures. To assess the perfusion of the human vessels, rhodamine UEA-I (20 µg per mouse; U8323; Solarbio, Beijing, China) was injected into the tail vein of the mice one week after implantation. Thirty minutes after injection, the mice were euthanized, and the explants were collected.

Statistical Analysis: Statistical analyses were performed using GraphPad Prism 10.1 software with the cut-off for statistical significance set at $p < 0.05$. For all cell culture and immunostaining experiments, statistical analysis was performed using Student's *t*-test for two-group comparisons and one-way analysis of variance (ANOVA) with post hoc Tukey tests to compare three or more groups. For statistics with both time and group factors, two-way ANOVA was used, followed by Tukey's or Sidak's multiple comparisons. Data were presented as mean ± standard deviation of the mean.

Supporting Information

Supporting Information is available from the Wiley Online Library or from the author.

Acknowledgements

D.S., K.Z., F.Z., and G.Y. contributed equally to this study. The authors were grateful to Drs. Liting Wang and Youlong Zeng for their support in conducting confocal imaging. The authors also express their gratitude to Drs. Daxue Zhou and Youying Huang for their support with the TEM. The authors thank Knorigene Technologies Co., Ltd. (Chongqing, China) for their assistance with single-cell sequencing analysis. The authors acknowledge financial support from the Key Projects of the National Natural Science Foundation of China (82230073), Natural Science Foundation of Chongqing (CSTB2024NSCQ-MSX0349), Open Project of Engineering Research Center of the Ministry of Education for Tissue and Organ Regeneration and Manufacturing (2023Jybgczx-zzqg005), Open Project of Chongqing Engineering Research Center of Organ Intelligent Bio-Manufacturing (CQERC-OIBM20241003), and Science and Technology Innovation Enhancement Project of Army Medical University (2022XQN01).

Conflict of Interest

The authors declare no conflict of interest.

Data Availability Statement

The data that support the findings of this study are available from the corresponding author upon reasonable request. The raw scRNA-seq data reported in this paper have been deposited in the Genome Sequence Archive in National Genomics Data Center, China National Center for Bioinformation / Beijing Institute of Genomics, Chinese Academy of Sciences (GSA-Human: HRA009054) that are publicly accessible at https://ngdc.cncb.ac.cn/gsa-human.

Keywords

angiogenesis, arteriole differentiation, blood vessel organoids, dynamic hydrogels, myocardial infarction, neovascularization, viscoelasticity

Received: July 24, 2024
Revised: December 4, 2024
Published online: December 17, 2024

[1] G. C. R. Consortium, C. Magnussen, F. M. Ojeda, D. P. Leong, J. Alegre-Diaz, P. Amouyel, L. Aviles-Santa, D. De Bacquer, C. M. Ballantyne, A. Bernabé-Ortiz, M. Bobak, H. Brenner, R. M. Carrillo-Larco, J. de Lemos, A. Dobson, M. Dörr, C. Donfrancesco, W. Drygas, R. P. Dullaart, G. Engström, M. M. Ferrario, J. Ferrières, G. de Gaetano, U. Goldbourt, C. Gonzalez, G. Grassi, A. M. Hodge, K. Hveem, L. Iacoviello, M. K. Ikram, et al., *N. Engl. J. Med.* **2023**, *389*, 1273.
[2] K. Thygesen, J. S. Alpert, A. S. Jaffe, B. R. Chaitman, J. J. Bax, D. A. Morrow, H. D. White, *Circulation* **2018**, *138*, e618.
[3] I.-E. Lupu, S. De Val, N. Smart, *Nat. Rev. Cardiol.* **2020**, *17*, 790.
[4] J. Zhang, R. Bolli, D. J. Garry, E. Marbán, P. Menasché, W.-H. Zimmermann, T. J. Kamp, J. C. Wu, V. J. Dzau, *J. Am. Coll. Cardiol.* **2021**, *78*, 2092.
[5] M. A. Laflamme, C. E. Murry, *Nature* **2011**, *473*, 326.
[6] A. Khand, M. Fisher, J. Jones, B. Patel, R. Perry, K. Mitsudo, *Am. Heart J.* **2013**, *166*, 941.
[7] H.-J. Cho, N. Lee, J. Y. Lee, Y. J. Choi, M. Ii, A. Wecker, J.-O. Jeong, C. Curry, G. Qin, Y. Yoon, *J. Exp. Med.* **2007**, *204*, 3257.
[8] A. Schuh, E. A. Liehn, A. Sasse, M. Hristov, R. Sobota, M. Kelm, M. W. Merx, C. Weber, *Basic Res. Cardiol.* **2008**, *103*, 69.
[9] M. A. Lancaster, J. A. Knoblich, *Science* **2014**, *345*, 1247125.
[10] J. Kim, B.-K. Koo, J. A. Knoblich, *Nat. Rev. Mol. Cell Biol.* **2020**, *21*, 571.
[11] R. A. Wimmer, A. Leopoldi, M. Aichinger, N. Wick, B. Hantusch, M. Novatchkova, J. Taubenschmid, M. Hammerle, C. Esk, J. A. Bagley, D. Lindenhofer, G. Chen, M. Boehm, C. A. Agu, F. Yang, B. Fu, J. Zuber, J. A. Knoblich, D. Kerjaschki, J. M. Penninger, *Nature* **2019**, *565*, 505.
[12] R. A. Wimmer, A. Leopoldi, M. Aichinger, D. Kerjaschki, J. M. Penninger, *Nat. Protoc.* **2019**, *14*, 3082.
[13] Y. Liu, Y. Zhang, T. Mei, H. Cao, Y. Hu, W. Jia, J. Wang, Z. Zhang, Z. Wang, W. Le, Z. Liu, *Adv. Sci.* **2022**, *9*, 2104299.
[14] K. Salewskij, J. M. Penninger, *Circ. Res.* **2023**, *132*, 498.
[15] M. A. Lancaster, J. A. Knoblich, *Nat. Protoc.* **2014**, *9*, 2329.
[16] S. L. Giandomenico, S. B. Mierau, G. M. Gibbons, L. M. D. Wenger, L. Masullo, T. Sit, M. Sutcliffe, J. Boulanger, M. Tripodi, E. Derivery, O. Paulsen, A. Lakatos, M. A. Lancaster, *Nat. Neurosci.* **2019**, *22*, 669.
[17] J. R. Spence, C. N. Mayhew, S. A. Rankin, M. F. Kuhar, J. E. Vallance, K. Tolle, E. E. Hoskins, V. V. Kalinichenko, S. I. Wells, A. M. Zorn, N. F. Shroyer, J. M. Wells, *Nature* **2011**, *470*, 105.
[18] S. Frenz-Wiessner, S. D. Fairley, M. Buser, I. Goek, K. Salewskij, G. Jonsson, D. Illig, B. zu Putlitz, D. Petersheim, Y. Li, P.-H. Chen, M. Kalauz, R. Conca, M. Sterr, J. Geuder, Y. Mizoguchi, R. T. A. Megens, M. I. Linder, D. Kotlarz, M. Rudelius, J. M. Penninger, C. Marr, C. Klein, *Nat. Methods* **2024**, *21*, 868.
[19] M. T. Kozlowski, C. J. Crook, H. T. Ku, *Commun. Biol.* **2021**, *4*, 1387.
[20] K. Zhang, Q. Feng, Z. Fang, L. Gu, L. Bian, *Chem. Rev.* **2021**, *121*, 11149.
[21] B. Yang, K. Wei, C. Loebel, K. Zhang, Q. Feng, R. Li, S. H. D. Wong, X. Xu, C. Lau, X. Chen, P. Zhao, C. Yin, J. A. Burdick, Y. Wang, L. Bian, *Nat. Commun.* **2021**, *12*, 3514.
[22] X. Xu, Q. Feng, X. Ma, Y. Deng, K. Zhang, H. S. Ooi, B. Yang, Z.-Y. Zhang, B. Feng, L. Bian, *Biomaterials* **2022**, *289*, 121802.

[23] C. O'Connor, E. Brady, Y. Zheng, E. Moore, K. R. Stevens, *Nat. Rev. Mater.* **2022**, *7*, 702.
[24] C. Sun, L. Wang, H. Wang, T. Huang, W. Yao, J. Li, X. Zhang, *Stem Cell Res. Ther.* **2020**, *11*, 149.
[25] Z. Xie, W. Yu, G. Ye, J. Li, G. Zheng, W. Liu, J. Lin, Z. Su, Y. Che, F. Ye, Z. Zhang, P. Wang, Y. Wu, H. Shen, *Exp. Mol. Med.* **2022**, *54*, 483.
[26] C. Mesa-Ciller, G. Turiel, A. Guajardo-Grence, A. B. Lopez-Rodriguez, J. Egea, K. De Bock, J. Aragonés, A. A. Urrutia, *J. Cereb. Blood Flow Metab.* **2023**, *43*, 44.
[27] Y.-H. Shih, D. Portman, F. Idrizi, A. Grosse, N. D. Lawson, *Development* **2021**, *148*, dev200189.
[28] A. C. Yang, R. T. Vest, F. Kern, D. P. Lee, M. Agam, C. A. Maat, P. M. Losada, M. B. Chen, N. Schaum, N. Khoury, A. Toland, K. Calcuttawala, H. Shin, R. Pálovics, A. Shin, E. Y. Wang, J. Luo, D. Gate, W. J. Schulz-Schaeffer, P. Chu, J. A. Siegenthaler, M. W. McNerney, A. Keller, T. Wyss-Coray, *Nature* **2022**, *603*, 885.
[29] E. A. Winkler, C. N. Kim, J. M. Ross, J. H. Garcia, E. Gil, I. Oh, L. Q. Chen, D. Wu, J. S. Catapano, K. Raygor, K. Narsinh, H. Kim, S. Weinsheimer, D. L. Cooke, B. P. Walcott, M. T. Lawton, N. Gupta, B. V. Zlokovic, E. F. Chang, A. A. Abla, D. A. Lim, T. J. Nowakowski, *Science* **2022**, *375*, eabi7377.
[30] M. Vanlandewijck, L. He, M. A. Mäe, J. Andrae, K. Ando, F. Del Gaudio, K. Nahar, T. Lebouvier, B. Laviña, L. Gouveia, Y. Sun, E. Raschperger, M. Räsänen, Y. Zarb, N. Mochizuki, A. Keller, U. Lendahl, C. Betsholtz, *Nature* **2018**, *554*, 475.
[31] A. Holm, T. Heumann, H. G. Augustin, *Trends Cell Biol.* **2018**, *28*, 302.
[32] H. van Splunder, P. Villacampa, A. Martínez-Romero, M. Graupera, *Trends Cell Biol.* **2024**, *34*, 58.
[33] Z. Wei, R. Schnellmann, H. C. Pruitt, S. Gerecht, *Cell Stem Cell* **2020**, *27*, 798.
[34] Z. Wei, M. Lei, Y. Wang, Y. Xie, X. Xie, D. Lan, Y. Jia, J. Liu, Y. Ma, B. Cheng, S. Gerecht, F. Xu, *Nat. Commun.* **2023**, *14*, 8307.
[35] M. Potente, H. Gerhardt, P. Carmeliet, *Cell* **2011**, *146*, 873.
[36] G. Eelen, L. Treps, X. Li, P. Carmeliet, *Circ. Res.* **2020**, *127*, 310.
[37] M. T. Nikolova, Z. He, R. A. Wimmer, M. Seimiya, J. M. Nikoloff, J. M. Penninger, J. G. Camp, B. Treutlein, *bioRxiv* **2022**.
[38] L. T. Ang, A. T. Nguyen, K. J. Liu, A. Chen, X. Xiong, M. Curtis, R. M. Martin, B. C. Raftry, C. Y. Ng, U. Vogel, A. Lander, B. J. Lesch, J. L. Fowler, A. R. Holman, T. Chai, S. Vijayakumar, F. P. Suchy, T. Nishimura, J. Bhadury, M. H. Porteus, H. Nakauchi, C. Cheung, S. C. George, K. Red-Horse, J. B. Prescott, K. M. Loh, *Cell* **2022**, *185*, 2523.
[39] A. Quillien, J. C. Moore, M. Shin, A. F. Siekmann, T. Smith, L. Pan, C. B. Moens, M. J. Parsons, N. D. Lawson, *Development* **2014**, *141*, 1544.
[40] L. Niklason, G. Dai, *Annu. Rev. Biomed. Eng.* **2018**, *20*, 431.
[41] K. Gaengel, G. Genové, A. Armulik, C. Betsholtz, *Arterioscler., Thromb., Vasc. Biol.* **2009**, *29*, 630.
[42] S. Das, A. B. Goldstone, H. Wang, J. Farry, G. D'Amato, M. J. Paulsen, A. Eskandari, C. E. Hironaka, R. Phansalkar, B. Sharma, S. Rhee, E. A. Shamskhou, D. Agalliu, V. de Jesus Perez, Y. J. Woo, K. Red-Horse, *Cell* **2019**, *176*, 1128.
[43] M. Han, Z. Liu, L. He, X. Li, L. Liu, X. Huang, M. Zhang, Y. Yan, K. O. Lui, B. Zhou, *Circulation* **2022**, *145*, 1179.
[44] D. Sun, L. Gong, J. Xie, X. Gu, Y. Li, Q. Cao, Q. Li, L. A., Z. Gu, H. Xu, *Sci. Bull.* **2018**, *63*, 907.
[45] K. Street, D. Risso, R. B. Fletcher, D. Das, J. Ngai, N. Yosef, E. Purdom, S. Dudoit, *BMC Genomics* **2018**, *19*, 477.
[46] X. Qiu, A. Hill, J. Packer, D. Lin, Y.-A. Ma, C. Trapnell, *Nat. Methods* **2017**, *14*, 309.

